



**HIGH HUMIDITY FABRICATION OF rGO INCORPORATED
PEROVSKITE ABSORBER AND MoS₂ ELECTRODE FOR
PROSPECTIVE INVERTED PSC**



DOCTOR OF PHILOSOPHY

2023



Faculty of Manufacturing Engineering



**HIGH HUMIDITY FABRICATION OF rGO INCORPORATED
PEROVSKITE ABSORBER AND MoS₂ ELECTRODE FOR
PROSPECTIVE INVERTED PSC**

Nur Ezyanie binti Safie

Doctor of Philosophy

2023

**HIGH HUMIDITY FABRICATION OF rGO INCORPORATED PEROVSKITE
ABSORBER AND MoS₂ ELECTRODE FOR PROSPECTIVE INVERTED PSC**

NUR EZYANIE BINTI SAFIE



UNIVERSITI TEKNIKAL MALAYSIA MELAKA

2023

DECLARATION

I declare that this thesis entitled “High Humidity Fabrication of rGO Incorporated Perovskite Absorber and MoS₂ Electrode for Prospective Inverted PSC” is the result of my own research except as cited in the references. The thesis has not been accepted for any degree and is not concurrently submitted in candidature of any other degree.

Signature :  : _____

Name : Nur Ezyanie Safie _____

Date : 28 September 2023 _____




APPROVAL

I hereby declare that I have read this thesis and in my opinion, this thesis is sufficient in terms of scope and quality for the award of the Doctor of Philosophy.

Signature

:



Supervisor Name

: Prof. Ir. Dr. Mohd Asyadi Azam Mohd Abid

Date

: 28 September 2023



DEDICATION

This thesis is dedicated to my parents for their boundless patience in seeing me fulfil my dreams to complete the highest education degree. Finally, I thank myself for not giving up on this beautiful roller coaster route.



ABSTRACT

Methylammonium lead triiodide (MAPbI_3) is a perovskite material that is widely used in perovskite solar cells due to its potential for high power conversion efficiency. However, it is sensitive to humid environments, heat, oxygen and UV radiation, which can cause it to degrade and negatively affect crystal growth and the morphology of the material. This can ultimately affect the efficiency of the solar cell. Therefore, MAPbI_3 is typically produced at a low humidity, which requires expensive equipment. The aim of this research study is to propose a facile fabrication process for fully solution-processable inverted perovskite solar cells employing reduced graphene oxide (rGO)-based material under high humidity conditions suitable for the weather in Malaysia. Overall, the research design was divided into three phases. The aim of phase 1 is to study the influence of incorporating sulfonated rGO (srGO) into the MAPbI_3 absorber layer for the deposition of a high-quality thin film under open-air conditions with high relative humidity. Three different samples were prepared with different weight percentage (wt%) of srGO: 0% (T), 50% (TS B) and 15% (TS D). The morphology of the srGO- MAPbI_3 films was improved by the addition of srGO, resulting in fewer defects and larger perovskite grain sizes approaching micron size. In phase 2, the study aimed to determine the optimal process parameter of molybdenum disulfide (MoS_2) composite with rGO as a viable solution-processed top electrode for an effective electron-collecting electrode by taking advantage of Taguchi analysis. The results of the Taguchi analysis showed that a ratio of rGO: MoS_2 (1:1), a heating temperature of 75°C , and a heating period of 15 minutes were the optimal parameters for the electrode manufacturing process. The discovered optimal parameters were deployed to fabricate rGO: MoS_2 composite electrode that showed a promising electrical conductivity of $9.36 \Omega/\text{sq}$. In phase 3, the device performance of the inverted perovskite solar cells with the designated configuration of ITO/CuSCN/srGO- MAPbI_3 /PCBM/BCP/rGO- MoS_2 was analyzed by numerical simulation with SCAPS-1D. The results proved that the device performance for the samples was affected by the addition of srGO to the absorber layer. The 15% srGO sample exhibited the highest PCE of 10.37% with Ag as the top electrode. However, when the conventional electrode was replaced with a rGO- MoS_2 composite electrode, the PCE of the same sample was improved to 13.23%, with a significant increase in FF. In summary, the findings of this research study indicate that incorporation of srGO into the MAPbI_3 absorber layer can improve the morphology of the srGO- MAPbI_3 films, resulting in fewer defects and larger perovskite grain sizes. The study also provides insight into the use of rGO- MoS_2 composite material as a workable solution-processed top electrode for an effective electron-collecting electrode, particularly in inverted configuration of perovskite solar cells. The numerical simulation results showed that the device performance of the samples could be improved by replacing Ag with rGO- MoS_2 . The findings of this study could have significant implications for the growth of cost-effective, solution-processed perovskite solar cells under high relative humidity.

FABRIKASI KELEMBAPAN TINGGI PENYERAP PEROVSKIT DAN ELEKTROD MoS_2 DIPERBADANKAN rGO UNTUK PROSPEKTIF PSC TERBALIK

ABSTRAK

Metilamonium plumbum triiodida (MAPbI_3) adalah bahan perovskit yang banyak digunakan dalam sel suria perovskit kerana berpotensi untuk kecekapan penukaran kuasa tinggi. Walau bagaimanapun, MAPbI_3 sensitif terhadap persekitaran lembap, panas, oksigen dan sinaran UV, yang boleh menyebabkannya merosot dan memberi kesan negatif terhadap pertumbuhan kristal dan morfologi bahan. Keadaan ini boleh mempengaruhi kecekapan sel suria. Oleh itu, MAPbI_3 biasanya dihasilkan pada kelembapan rendah, yang memerlukan peralatan yang mahal. Tujuan kajian penyelidikan ini adalah untuk mencadangkan proses fabrikasi yang mudah untuk sel suria perovskit terbalik yang dapat diproses sepenuhnya menggunakan bahan berasaskan grafen oksida yang dikurangkan (rGO) dalam keadaan kelembapan tinggi yang sesuai untuk cuaca di Malaysia. Secara keseluruhan, reka bentuk penyelidikan dibahagikan kepada tiga fasa. Tujuan fasa 1 adalah untuk mengkaji pengaruh penggabungan rGO sulfonat (srGO) ke dalam lapisan penyerap MAPbI_3 untuk pemendapan filem nipis berkualiti tinggi dalam keadaan terbuka dengan kelembapan relatif yang tinggi. Tiga sampel berbeza disediakan dengan peratusan berat yang berbeza (wt%) srGO: 0% (T), 50% (TS B) dan 15% (TS D). Morfologi filem srGO- MAPbI_3 diperbaiki dengan penambahan srGO, menghasilkan ukuran butiran perovskit yang lebih besar mendekati ukuran mikron. Pada fasa 2, kajian ini bertujuan untuk menentukan parameter proses optimum bagi menghasilkan gabungan komposit antara molibdenum disulfida (MoS_2) dengan rGO sebagai elektrod teratas yang diproses untuk pengumpulan elektron yang berkesan dengan memanfaatkan kaedah analisis Taguchi. Hasil analisis Taguchi menunjukkan bahawa nisbah rGO: MoS_2 (1:1), suhu pemanasan 75°C , dan tempoh pemanasan 15 minit adalah parameter optimum untuk proses pembuatan elektrod ini. Parameter optimum yang ditemui digunakan untuk membuat elektrod komposit rGO: MoS_2 yang menunjukkan kekonduksian elektrik yang baik iaitu $9.36 \Omega/\text{meter}$ persegi. Pada fasa 3, prestasi peranti sel suria perovskite terbalik dengan konfigurasi yang ditentukan iaitu ITO/ $\text{CuSCN}/\text{srGO}-\text{MAPbI}_3/\text{PCBM}/\text{BCP}/\text{rGO}-\text{MoS}_2$ dianalisis dengan simulasi SCAPS-1D. Hasilnya membuktikan bahawa prestasi peranti untuk sampel kajian dipengaruhi oleh penambahan srGO ke lapisan penyerap MAPbI_3 . Sampel srGO 15% menunjukkan nilai PCE tertinggi iaitu 10.37% dengan Ag sebagai elektrod teratas. Walau bagaimanapun, apabila elektrod konvensional itu digantikan dengan elektrod komposit rGO- MoS_2 , PCE sampel yang sama ditingkatkan menjadi 13.23%, dengan peningkatan FF yang ketara. Ringkasnya, penemuan kajian penyelidikan ini menunjukkan bahawa penggabungan srGO ke dalam lapisan penyerap MAPbI_3 dapat meningkatkan morfologi filem srGO- MAPbI_3 , mengakibatkan ukuran butiran perovskit menjadi lebih besar. Kajian ini juga memberikan gambaran mengenai penggunaan bahan komposit rGO- MoS_2 sebagai elektrod atas yang dapat dilaksanakan untuk menjadi elektrod pengumpul elektron yang berkesan, terutama dalam konfigurasi terbalik sel suria perovskit. Hasil simulasi berangka menunjukkan bahawa prestasi peranti sampel dapat ditingkatkan dengan menggantikan Ag dengan rGO- MoS_2 . Penemuan kajian ini boleh memberi implikasi yang signifikan terhadap pertumbuhan sel suria perovskit yang diproses dengan kos efektif di bawah kelembapan relatif yang tinggi.

ACKNOWLEDGEMENTS

In the Name of Allah, the Most Gracious, the Most Merciful

First and foremost, I thank and praise Allah the Almighty, my Creator, my Sustainer, for everything I have received since the beginning of my life. I want to extend my appreciation to the Universiti Teknikal Malaysia Melaka (UTeM) for providing the research platform, facilities support and UTeM Zamalah Scheme for financial assistance.

My utmost appreciation goes to my main supervisor, Prof. Ir. Dr. Mohd Asyadi 'Azam Mohd Abid, Fakulti Kejuruteraan Pembuatan, Universiti Teknikal Malaysia Melaka (UTeM), for all his support, advice, and inspiration. His constant patience in guiding and providing priceless insights will forever be remembered. Also, to my co-supervisor, Prof. Ts. Dr. Joseph Sahaya Anand Thangaraj, Fakulti Teknologi Kejuruteraan Mekanikal dan Pembuatan, Universiti Teknikal Malaysia Melaka (UTeM), who constantly supported my journey. My deep appreciation also goes to Assoc. Prof. Dr. Norasikin Ahmad Ludin, Solar Energy Research Institute, Universiti Kebangsaan Malaysia (UKM), and assistant engineers in Makmal B, Fakulti Kejuruteraan Pembuatan, Universiti Teknikal Malaysia Melaka (UTeM) for all the help and support I received from them.

Last but not least, from the bottom of my heart, gratitude to my beloved husband, Ts. Dr. Noorrezam Yusop, for his encouragement and who has been the pillar of strength in all my endeavors. My eternal love also to my daughter, Nawwal Erina Noorrezam, for her patience and understanding. I also want to thank my beloved parents and family for their endless support, love, and prayers. Finally, thank you to all the individuals, especially fellow postgraduate members who provided me with the assistance, support, and inspiration to embark on my study.

TABLE OF CONTENTS

	PAGE
DECLARATION	
APPROVAL	
DEDICATION	
ABSTRACT	i
ABSTRAK	ii
ACKNOWLEDGEMENTS	iii
TABLE OF CONTENTS	iv
LIST OF TABLES	vii
LIST OF FIGURES	ix
LIST OF SYMBOLS AND ABBREVIATIONS	xvii
LIST OF APPENDICES	xix
LIST OF PUBLICATIONS	xx
CHAPTER 1 INTRODUCTION	1
1.1 Background	1
1.2 Problem Statements	5
1.3 Research Objective	7
1.4 Scope of Research	7
1.5 Limitation of Research	9
1.6 Significance of Research	10
1.7 Thesis Outline	10
CHAPTER 2 LITERATURE REVIEW	13
2.1 Introduction	13
2.2 Perovskite Solar Cells	14
2.2.1 Device Architecture of Perovskite Solar Cell	15
2.2.2 Device Components and Operating Principle	17
2.2.3 State-of-the-art for Perovskite Solar Cells	20
2.3 Graphene-based Materials	21
2.4 Perovskite Material	25
2.4.1 Adaptation of Graphene-based Materials in Various Perovskite Material	27
2.5 Electron Transport Materials (ETM)	30
2.5.1 Adaptation of Graphene-based Materials in Various ETM	32

2.5.1.1	Titanium dioxide (TiO ₂)	32
2.5.1.2	Zinc Oxide (ZnO)	38
2.5.1.3	Tin Oxide (SnO ₂)	41
2.5.1.4	[6,6]-Phenyl-C61-butyric acid methyl ester (PCBM)	44
2.6	Hole Transport Material (HTM)	46
2.6.1	Adaptation of Graphene-based materials in Various HTM	47
2.6.1.1	Spiro-OMeTAD	47
2.6.1.2	Poly (3,4-ethylenedioxythiophene)polystyrene sulfonate (PEDOT: PSS)	48
2.6.1.3	Copper (I) Thiocyanate	50
2.6.1.4	Graphene-based Material Acts as a Stand-alone HTM	53
2.7	Top Electrode	67
2.7.1	Adaptation of Graphene-based Materials as Top Electrode	68
2.8	Material Characterization based on Literature	69
2.8.1	Crystallographic Structure Analysis via Diffraction Techniques	70
2.8.2	Micro- and Nano- Structural Features via Microscopy Technique	72
2.8.3	Material Determination via Spectroscopy Technique	73
2.9	Electrical Properties of Thin Film and Device Performance	78
2.9.1	Sheet Resistance Measurement Using the Four-Probe Method	78
2.9.2	Current-Voltage (<i>I-V</i>) Characteristics of Solar Device	79
2.10	Summary	80
CHAPTER 3 METHODOLOGY		82
3.1	Introduction	82
3.2	Research Design	82
3.2.1	Experimental Setup for Phase 1: Investigation of srGO-Doped MAPbI ₃ in an Open Air under High Relative Humidity	85
3.2.1.1	Synthesis of Reduced Graphene Oxide (rGO)	85
3.2.1.2	Synthesis of Sulfonated rGO (srGO)	86
3.2.1.3	Preparation of srGO-Doped MAPbI ₃ Thin Film	86
3.2.2	Experimental Setup for Phase 2: Determination of Optimum Parameter for Preparation of rGO-MoS ₂ Top Electrode	89
3.2.2.1	Synthesis of rGO-MoS ₂ composite	89
3.2.2.2	Preparation of rGO-MoS ₂ top electrode	90
3.2.2.3	Design of Experiment via Taguchi Technique	91
3.2.3	Experimental Setup for Phase 3: Fabrication of rGO-based Inverted Perovskite Solar Cells	93
3.2.3.1	Device Fabrication Process	94
3.3	Material Characterization and Analysis	95
3.3.1	X-Ray Diffraction (XRD)	95
3.3.2	Raman Spectroscopy	96
3.3.3	Photoluminescence (PL) and Time-Resolved Photoluminescence (TRPL) Spectroscopy	97
3.3.4	Fourier-Transform Infrared Spectroscopy (FTIR)	98
3.3.5	Field Emission Scanning Electron Microscopy (FESEM)	99
3.3.6	Ultraviolet-visible (UV-Vis) Spectroscopy	100
3.4	Electrical Properties and Device Performance Measurement	100

3.4.1	Electrical Conductivity Calculation via Four-Point Probe (FPP) Measurement	100
3.4.2	Current-Voltage (<i>I-V</i>) Curve Measurement	101
3.4.3	SCAPS-1D	102
3.5	Summary	103
CHAPTER 4 RESULTS AND DISCUSSION		104
4.1	Introduction	104
4.2	Phase 1: Investigation of srGO-Doped MAPbI ₃ in an Open Air under High Relative Humidity	105
4.2.1	Preliminary Work and Challenge to Air-fabricate MAPbI ₃ at above 80% Relative Humidity	105
4.2.2	Structural and Morphological Properties of rGO and srGO	110
4.2.2.1	FTIR Analysis	111
4.2.2.2	Raman Analysis	112
4.2.2.3	XRD Analysis	115
4.2.2.4	FESEM and EDX Analysis	118
4.2.3	Effect of srGO as Dopant for MAPbI ₃ Growth at Above 80% Relative Humidity	121
4.2.3.1	Structural and Morphological Study of srGO-MAPbI ₃ Absorber Material	121
4.2.3.2	Optoelectronic Properties of srGO-MAPbI ₃	127
4.3	Phase 2: Study of rGO-MoS ₂ Composite as Electrode	134
4.3.1	Preliminary Work to Determine Type of Binder and Carbon Conductive Filler for Electrode Slurry	134
4.3.2	Determination of Optimum Parameter for rGO-MoS ₂ Electrode Fabrication Process via Taguchi Technique	136
4.3.3	Structural and Morphological Properties of rGO-MoS ₂ Composite	141
4.3.3.1	Raman Analysis	142
4.3.3.2	XRD Analysis	144
4.3.3.3	FESEM Analysis	145
4.3.4	Optical and Electrical Properties of rGO-MoS ₂ Top Electrode	149
4.3.4.1	Optical Band Gap Calculation from UV-Vis Analysis	149
4.3.4.2	Electrical Conductivity Calculation from FPP measurement	151
4.4	Phase 3: Fabrication of rGO-based Inverted Perovskite Solar Cells	154
4.4.1	Challenges of Air-fabricated Inverted Perovskite Solar Cells at High Relative Humidity	154
4.4.2	Simulation Analysis of Experimentally Design rGO-based Inverted Perovskite Solar Cell	158
4.5	Summary	164
CHAPTER 5 CONCLUSION AND RECOMMENDATIONS		165
5.1	Conclusion	165
5.2	Recommendations	168
REFERENCES		170
APPENDICES		203

LIST OF TABLES

TABLE	TITLE	PAGE
Table 2.1	Summary of the graphene-based perovskite solar cells in terms of photovoltaic performance and device performance stability	59
Table 3.1	Ratio distribution of TBAI with srGO	87
Table 3.2	Compositition of rGO and MoS ₂	90
Table 3.3	Control factors and their levels for Taguchi's L ₉ experiment	91
Table 3.4	Noise factor and its levels for Taguchi's L ₉ experiment	92
Table 3.5	Taguchi's L ₉ orthogonal array (OA) for optimization of rGO-MoS ₂ top electrode fabrication method	93
Table 4.1	Raman parameters for rGO and srGO	115
Table 4.2	Summarized of XRD parameter for rGO and srGO	117
Table 4.3	Summarizes of EDX parameter for rGO and srrGO	119
Table 4.4	PL peak position and summary of the parameter from fitting TRPL decay	134
Table 4.5	Sheet resistance value for rGO-based electrode thin film with different type of binder and carbon conductive filler	135
Table 4.6	Sheet resistance value for rGO-MoS ₂ composite electrode film.	137
Table 4.7	noise parameter	138
Table 4.8	Result of ANOVA and the best setting of control factors	139
Table 4.9	Sheet resistance value upon confirmation test	141
Table 4.10	Raman parameters for rGO:MoS ₂ with three different ratio (1:1, 1:3, and 3:1), pristine rGO, and pristine MoS ₂	142

Table 4.11	Average cross-sectional thickness of rGO-MoS ₂ composite electrode thin film	146
Table 4.12	Electrical conductivity value for rGO-MoS ₂ electrode thin film	151
Table 4.13	Device performance of TS D and TS B with Ag and rGO-MoS ₂ electrode fabricated in this study	154
Table 4.14	Simulation parameters for inverted perovskite solar cell with device configuration of ITO/CuSCN/srGO-MAPbI ₃ /PCBM/BCP/Ag	159
Table 4.15	Simulated device performance parameter for ITO/CuSCN/srGO-MAPbI ₃ /PCBM/BCP/Ag	160
Table 4.16	Device Simulation parameter	162
Table 4.17	Simulated device performance parameter for ITO/CuSCN/srGO-MAPbI ₃ /PCBM/BCP/Ag and ITO/CuSCN/srGO-MAPbI ₃ /PCBM/BCP/rGO-MoS ₂	163

LIST OF FIGURES

FIGURE	TITLE	PAGE
Figure 1.1	Classification of photovoltaic generations	1
Figure 1.2	Cell efficiency chart for the best research including all generations of solar cells reported by National Renewable Energy Laboratory. Extracted in 2022. (https://www.nrel.gov/pv/cell-efficiency.html)	4
Figure 2.1	Illustration of perovskite solar cell components comprises a perovskite active layer sandwiched between ETL and HTL with corresponding electrodes in direct and inverted architecture (vertical) as well as planar and mesoscopic structure (horizontal). ETL, electron transport layer; HTL, hole transport layer	16
Figure 2.2	Energy levels of various common HTMs and ETMs together with iodide and bromide-based halide-perovskites	18
Figure 2.3	A schematic illustration of possible ways for the preparation of graphene and rGO (Rowley-Neale et al., 2018)	23
Figure 2.4	Schematic illustration of synthesis techniques to produce no-oxidation GQDs (no-ox-GQDs), low-oxidation GQDs (low-ox-GQDs), medium-oxidation GQDs (med-ox-GQDs), and high-oxidation GQDs (high-ox-GQDs) (Jeong et al., 2020)	24
Figure 2.5	ABX ₃ perovskite structure (Santomauro et al., 2017)	26

Figure 2.6	(a) and (b) Pristine perovskite layer before annealing. (c) and (d) Perovskite with graphene nanofibers before annealing. (e) Pristine perovskite layer after annealing. (f) Perovskite layer with graphene nanofibers after annealing (Li and Leung, 2018)	29
Figure 2.7	Normalized (A) Voc, (B) Jsc, (C) FF, and (D) PCE trends versus time under prolonged 1 sun illumination at maximum power point (MPP) polarization provided by a calibrated white light emitting diode (LED) for devices A-D (A: without graphene; B: GO-based device; C: G-doped TiO ₂ -based device; D: GO/G-doped TiO ₂ -based device) (Agresti et al., 2016)	34
Figure 2.8	Schematic illustration of perovskite solar cell having an architecture of FTO/N-doped graphene-ZnO NR composite/MAPbI ₃ /Spiro-OMeTAD/Ag (Chandrasekhar, Dubey and Qiao, 2020)	39
Figure 2.9	(a) <i>I</i> – <i>V</i> curves measured at the reverse, and forward scans; (b) EQE spectra; (c) stabilized PCEs measured as a function of time, and (d) normalized time-resolved photoluminescence response of the SnO ₂ and graphene-SnO ₂ ETLs (Zhu et al., 2018)	42
Figure 2.10	Performances of the devices with PCBM and PCBM: GQDs ETL under continuous solar illumination in the glove box and measured in air (~45% relative humidity) (Yang et al., 2017)	46

Figure 2.11	Scanning electron microscope (SEM) top view images of MAPbI ₃ films on: (a) ITO/rGO; (b) ITO/rGO/CuSCN; (c) steady-state PL measurement of the MAPbI ₃ on top of glass, ITO/rGO, and ITO/rGO/CuSCN; and (d) energy level diagram of the fabricated perovskite solar cell	52
Figure 2.12	SEM images of MAPbI ₃ films on: (a) glass/ITO/PEDOT:PSS; (b) glass/ITO/rGO; (c) time-resolved PL characteristics of the MAPbI ₃ films based on different HTMs; (d) photoluminescence responses of MAPbI ₃ films on glass/ITO/PEDOT:PSS, glass/ITO/GO, and glass/ITO/rGO (Yeo et al., 2015)	55
Figure 2.13	Transmission electron microscope (TEM) images for perovskite films deposited on: (A) PEDOT:PSS; and (B) MFGO HTLs; and (C) contact angles of water droplets on the different ITO/HTL substrates (Yeo et al., 2016)	58
Figure 2.14	XRD spectra of MoS ₂ -rGO composite (above) and MoS ₂ (below) (Faraz, Singh and Khare, 2022)	72
Figure 2.15	FESEM images of graphene nanoplatelets at different magnification (Azam, Mudtalib and Seman, 2018)	73
Figure 2.16	Raman spectra variation according to the material's structure based on the synthesized method employed. (graphite denoted as GR; freeze-dried graphene oxide denoted as GOlyo; thermally reduced graphene oxides denoted as TRGO; and	

	chemically reduced graphene oxides denoted as CRGO) (Farah et al., 2020)	75
Figure 2.17	FTIR spectra for graphene-based materials. a) Graphite b) Graphene Oxides c) Reduced Graphene Oxide (Bychko et al., 2022)	75
Figure 2.18	a) UV-vis spectra; b-c) Tauc plot utilized to calculate band gap (Fei et al., 2015)	77
Figure 2.19	a) PL and b)TRPL spectra (Wathage et al., 2017)	78
Figure 2.20	Schematic diagram of four-point probe tools (Naftaly et al., 2021)	79
Figure 2.21	Example of <i>I-V</i> Characteristics	80
Figure 3.1	Flow chart of the experimental work	84
Figure 3.2	Schematic device structure of inverted perovskite solar cells fabricated in this study	94
Figure 4.1	Top view of SEM image for ITO/CuSCN/MAPbI ₃ fabricated by two-step spin coating process with differently modified technique. a) Conventional two-step spin coating technique b) Modified with preheat technique c) Modified with ethyl acetate as anti-solvent d) Modified with PMMA as polymer encapsulation of perovskite layer	109
Figure 4.2	Top view of a) SEM image of ITO/CuSCN/MAPbI ₃ fabricated by two-step spin coating process with TBAI as an additive b) FESEM image of ITO/CuSCN/MAPbI ₃ fabricated by two-step	

	spin coating process with sequential prenucleation technique	
	and TBAI as an additive	109
Figure 4.3	FTIR spectra of rGO and srGO	112
Figure 4.4	Raman spectra of rGO and srGO	114
Figure 4.5	XRD pattern of synthesized rGO and srGO	117
Figure 4.6	FESEM image of a) rGO and b) srGO nanosheets synthesized	
	in this study	119
Figure 4.7	FESEM image and EDX pattern for (a-b) srGO (c-d) rGO	
	synthesized in this study	120
Figure 4.8	Illustration of srGO role to improve MAPbI ₃ growth with the	
	interaction between sulfonate anion (-SO ₃ ⁻) and	
	methylammonium cation (MA ⁺)	121
Figure 4.9	(a) XRD patterns of srGO-MAPbI ₃ perovskite films with	
	different srGO wt% denoted as T(0%), TS B(50%), TS	
	C(25%), TS D(15%), and TS E(5%) (# - PbI ₂ , * - perovskite	
	phase (cubic)) (b) the zoomed XRD patterns of sample T, TS	
	B, and TS C at the 2θ range of 5°-9°	123
Figure 4.10	(a, c and e) FESEM images of a srGO-MAPbI ₃ film with	
	different wt% ratio of srGO, denoted as T (0%), TS B (50%),	
	and TS D (15%). (Scale bar is the same for all images). (b, d	
	and f) Perovskite grain size distribution from FESEM image.	
	The number of grains calculated for the average is 100. Yellow	
	circles indicate the surface and point defects	126

Figure 4.11	Comparison of perovskite's grain size distribution from FESEM images of srGO-MAPbI ₃ film with different wt% ratio of srGO, denoted as T (0%), TS B (50%), and TS D (15%). The number of grains calculated for average is 100	127
Figure 4.12	Absorbance spectra of srGO-MAPbI ₃ film with different wt% ratio of srGO, denoted as T (0%), TS B (50%), and TS D (15%)	129
Figure 4.13	Tauc plot of srGO-MAPbI ₃ film with different wt% ratio of srGO, denoted as T (0%), TS B (50%), and TS D (15%)	130
Figure 4.14	Steady state PL spectra of ITO/CuSCN/srGO-MAPbI ₃ with different wt% ratio of srGO, denoted as T (0%), TS B (50%), and TS D (15%)	132
Figure 4.15	TRPL decay curve of ITO/CuSCN/srGO-MAPbI ₃ with different wt% ratio of srGO, denoted as T (0%), TS B (50%), and TS D (15%)	133
Figure 4.16	Factor effect (FE) plot for SNR (Smaller-the-Better) of sheet resistance for rGO-MoS ₂ electrode	140
Figure 4.17	Raman spectra of a) rGO-MoS ₂ composite with three different wt% ratio denoted as 1:1, 1:3, and 3:1 (b) pristine MoS ₂ c) pristine rGO	143
Figure 4.18	XRD spectra of rGO-MoS ₂ composites, pure rGO, and pure MoS ₂	145
Figure 4.19	(a and c) Backscattered FESEM image at 10 μm and 1 μm scale bars, (b and d) FESEM image at 10 μm and 1 μm scale	

	bars for cross-section of a rGO:MoS ₂ (1:1) composite electrode fabricated on ITO glass	147
Figure 4.20	(a and c) Backscattered FESEM image at 10 μm and 1 μm scale bars, (b and d) FESEM image at 10 μm and 1 μm scale bars for cross-section of a rGO:MoS ₂ (1:3) composite electrode fabricated on ITO glass	147
Figure 4.21	(a and c) Backscattered FESEM image at 10 μm and 1 μm scale bars, (b and d) FESEM image at 10 μm and 1 μm scale bars for cross-section of a rGO:MoS ₂ (3:1) composite electrode fabricated on ITO glass	148
Figure 4.22	Cross-sectional thickness of rGO-MoS ₂ composite electrode thin film at three different spot	148
Figure 4.23	(a) Absorption spectra and (b and c) Tauc plot for pristine rGO and MoS ₂	150
Figure 4.24	(a) Absorption spectra and (b - d) Tauc plot for pristine rGO:MoS ₂ composites at different wt% ratio	150
Figure 4.25	Illustration of mechanism for electron pathway in rGO-MoS ₂ composite electrode	153
Figure 4.26	Cross-section of FESEM images for inverted perovskite solar cell fabricated in this study with Ag electrode	155
Figure 4.27	Cross-section of the FESEM image of inverted perovskite solar cell fabricated in this study with rGO-MoS ₂ composite electrode	155

Figure 4.28	Cross-section of FESEM images for inverted perovskite solar cell fabricated in this study. Yellow circle marked the defects and detected at interface layer	156
Figure 4.29	(a) Current-voltage characteristics of ITO/CuSCN/srGO-MAPbI ₃ /PCBM/BCP/Ag (b) Relation of srGO wt% ratio to device performance parameter	160
Figure 4.30	Current-voltage characteristics of ITO/CuSCN/srGO-MAPbI ₃ /PCBM/BCP/Ag and ITO/CuSCN/srGO-MAPbI ₃ /PCBM/BCP/rGO-MoS ₂	163



LIST OF SYMBOLS AND ABBREVIATIONS

0D	-	Zero Dimensional
1D	-	One Dimensional
2D	-	Two Dimensional
3D	-	Three Dimensional
Ag	-	Silver
Al	-	Aluminium
Au	-	Gold
BCP	-	Bathocuproine
CB	-	Conduction Band
CuSCN	-	Copper Thiocyanate
CVD	-	Chemical Vapour Deposition
E_g^{opt}	-	Optical Bandgap
ETL	-	Electron Transport Layer
ETM	-	Electron Transport Material
eV	-	Electron Volt
FESEM	-	Field Emission Scanning Electron Microscopy
FF	-	Fill Factor
FTIR	-	Fourier-Transform Infrared Spectroscopy
FTO	-	Flourine-doped Tin Oxide
GO	-	Graphene Oxide
GQD	-	Graphene Quantum Dot
HOMO	-	Highest Occupied Molecular Orbital
HTL	-	Hole Transport Layer
HTM	-	Hole Transport Material
I-V	-	Current-Voltage
J_{sc}	-	Short Circuit Current Density
Li-TFSI	-	Li-bis(trifluoromethanesulfonyl)
LUMO	-	Lowest Unoccupied Molecular Orbital
mA/cm^2	-	MiliAmpere per Centimeter Square

MAPbBr ₃	-	Methylammonium Lead Bromide
MAPbI ₃	-	Methylammonium Lead Triiodide
MoS ₂	-	Molybdenum Disulfide
n-i-p	-	Negative-Intrinsic-Positive
nm	-	Nanometer
PCBM	-	[6,6]-phenyl-C ₆₁ -butyric acid methyl ester
PCE	-	Power Conversion Efficiency
PEDOT:	-	Poly(3,4-ethylene dioxythiophene) polystyrene sulfonate
PSS		
p-i-n	-	Positive-Intrinsic-Negative
PL	-	Photoluminescence
R _{ct}	-	Charge Transfer Resistance
rGO	-	Reduced Graphene Oxide
SCAPS	-	Solar Cell Capacitance Simulator
SnO ₂	-	Tin Oxide
spiro-	-	2,2',7,7'-tetrakis(N,N-di-p-methoxyphenylamine)-9,9'-
OMeTAD		spirobifluorene
srGO	-	Sulfonated Reduced Graphene Oxide
TBP	-	Tert-butylpyridine
TCO	-	Transparent Conducting Oxides
TiO ₂	-	Titanium Dioxide
TRPL	-	Time-Resolved Photoluminescence
UV-Vis	-	Ultraviolet-visible Spectroscopy
V	-	Voltage
VB	-	Valence Band
V _{oc}	-	Open Circuit Voltage
XRD	-	X-Ray Diffraction
ZnO	-	Zinc Oxide